Analysis of Tipping-Curve Measurements Performed at the DSS-13 Beam-Waveguide Antenna at 32.0 and 8.45 Gigahertz

D. D. Morabito
Communications Systems and Research Section

L. Skjerve
Tracking Systems and Applications Section

This article reports on the analysis of the Ka-band Antenna Performance Experiment tipping-curve data acquired at the DSS-13 research and development beam-waveguide (BWG) antenna. By measuring the operating system temperatures as the antenna is moved from zenith to low-elevation angles and fitting a model to the data, one can obtain information on how well the overall temperature model behaves at zenith and approximate the contribution due to the atmosphere. The atmospheric contribution estimated from the data can be expressed in the form of (1) atmospheric noise temperatures that can provide weather statistic information and be compared against those estimated from other methods and (2) the atmospheric loss factor used to refer efficiency measurements to zero atmosphere. This article reports on an analysis performed on a set of 68 8.4-GHz and 67 32-GHz tipping-curve data sets acquired between December 1993 and May 1995 and compares the results with those inferred from a surface model using input meteorological data and from water vapor radiometer (WVR) data. The general results are that, for a selected subset of tip curves, (1) the BWG tipping-curve atmospheric temperatures are in good agreement with those determined from WVR data (the average difference is 0.06 ± 0.64 K at 32 GHz) and (2) the surface model average values are biased 3.6 K below those of the BWG and WVR at 32 GHz.

I. Introduction

Several studies in DSN telecommunications have shown that by utilizing 32-GHz frequencies (31.8–32.3 GHz, Ka-band) over 8.4 GHz (8.4–8.45 GHz, X-band) on a spacecraft-to-ground communications link, an advantage of 6 to 8 dB can be realized for a given spacecraft telecommunications system [1,2]. The advantage comes from increased antenna gain at the smaller wavelengths, but it is also reduced by higher atmospheric noise, antenna performance deficiencies, and weather susceptibility at 32 GHz.

The concept of conducting a 32-GHz link experiment to verify these studies and to discover any impediments that could deter this gain from being realized was proposed by Riley et al. [3]. The first

experiment planned was for Mars Observer to carry a small Ka-band transmitter on board; this became reality with the first Ka-band Link Experiment (KaBLE) experiments [4]. KaBLE ended with the loss of Mars Observer in August 1993.

The Ka-band Antenna Performance Experiment (KaAP) was initiated to observe natural radio sources at both Ka-band and 8.4 GHz in order to characterize this link advantage at DSS 13 and to characterize the gain or efficiency of the antenna at both bands as improvements and configuration changes are implemented. The KaAP experiment consists of observing natural calibrator radio sources over the sky, usually one to two tracks per month, with each track typically being 8 to 16 hours in duration. Each track consists of performing a series of boresight observations over different radio sources at 32 and 8.4 GHz. Each individual observation consists of stepping the antenna beam over the radio source in two orthogonal directions. The radio source temperature is measured by fitting linearized Gaussians over the boresight data [5]. The source temperatures are converted to efficiencies by using an equation that includes (1) the source's known flux strength, (2) a factor to correct for the source's angular extent over the antenna beam, (3) the atmospheric loss factor, and(4) a correction for any system nonlinearity. In addition to the boresight observations, system calibrations are routinely conducted to calibrate out gain changes as the experiment progresses and to allow the system nonlinearity (usually very small) to be determined. A detailed discussion of the system calibration methodology is provided in [6]

In addition to the boresight observations and system gain/linearity calibrations, a sequence of observations, known as tip curves, that characterizes the effect of the atmosphere during the data-acquisition period is performed. These tip curves provide a measure of the atmospheric noise temperatures (used in statistical characterizations) and atmospheric loss factors (used in the efficiency determination). The atmospheric noise-temperature measurements and their statistics can also be compared with those determined from a surface model using input meteorological data and from water vapor radiometer (WVR) data.

This article focuses on the data analysis of the tip-curve measurements performed during the KaAP experiments and describes the DSS-13 antenna and system used to acquire the measurements, the data-acquisition technique and model used to fit the data, the results obtained from the tip-curve data, including comparisons with surface-model and WVR data, and suggested recommendations for future studies.

II. Ground Station and Equipment

The research and development (R&D) 34-m beam-waveguide (BWG) antenna at DSS 13 in Goldstone, California, is shown in Fig. 1. The locations of focal points and mirror configurations are presented in Fig. 2. This antenna was developed in two phases. In phase I, the antenna was designed, constructed, and tested for performance at 8.4 GHz and Ka-band. In phase II, the antenna was transformed into a functioning tracking station for KaBLE under a set of requirements given in [4]. The station was required to simultaneously track the dual X-/Ka-band signals from Mars Observer, demodulate and decode the telemetry, and store the relevant tracking statistics for future analysis.

A block diagram of the configuration for the KaAP system as it is currently realized for natural radio source observations is shown in Fig. 3. The ground station system can be described in terms of several subsystems: antenna microwave, receiver, data acquisition, monitor and control, and frequency and timing. Each subsystem will be described briefly below.

A. Antenna Subsystem

The pointing subsystem at the 32-GHz band requires more accurate pointing when tracking objects than it does at 8.4 GHz. Whereas an accuracy of 8 mdeg for 8.4 GHz is sufficient, for KaAP an accuracy of 2 mdeg is required to limit pointing loss to less than 0.5 dB [4]. Pointing calibrations had been shown

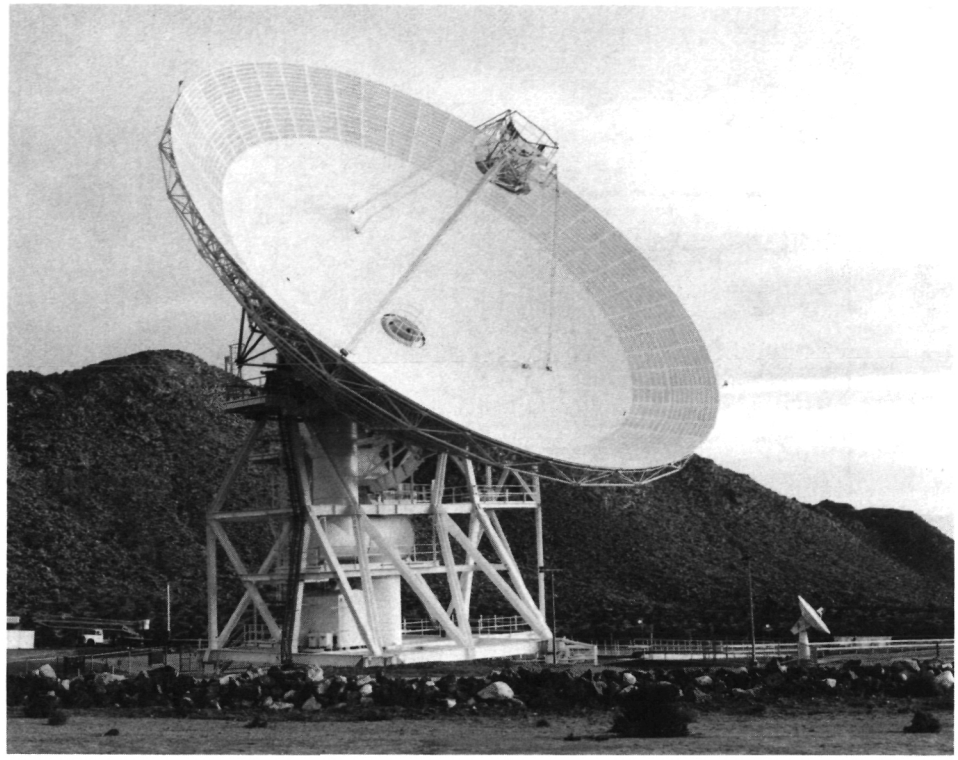

Fig. 1. DSS-13 34-m beam-waveguide antenna.

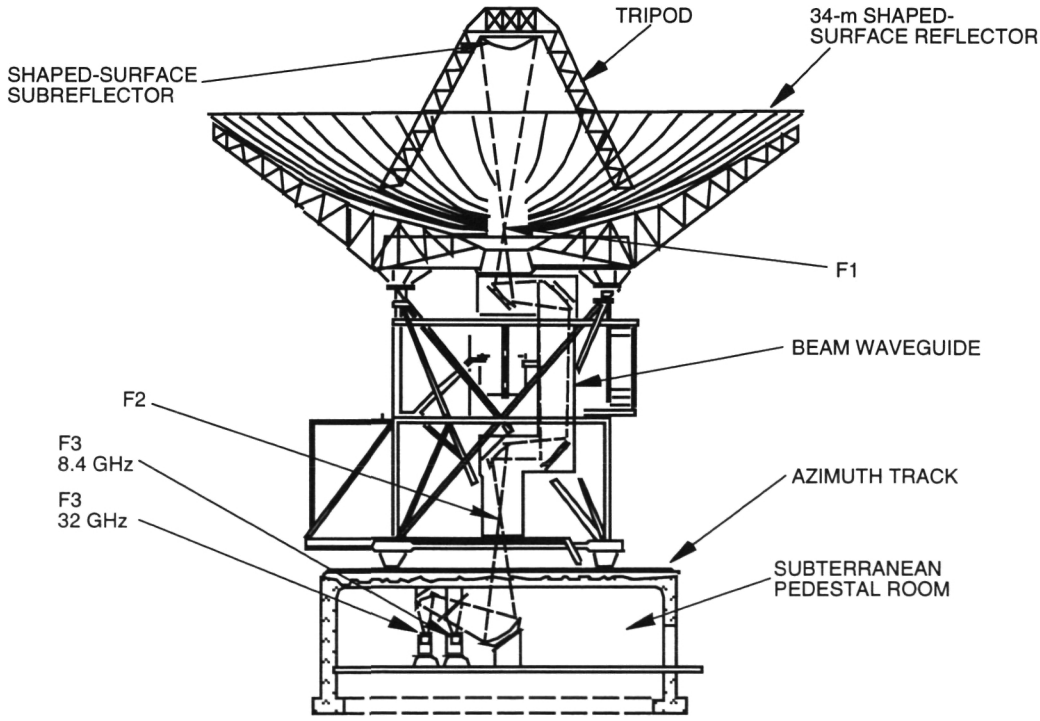

Fig. 2. Geometric configuration of reflectors and mirrors of DSS-13 BWG antenna along with positions of focal points.

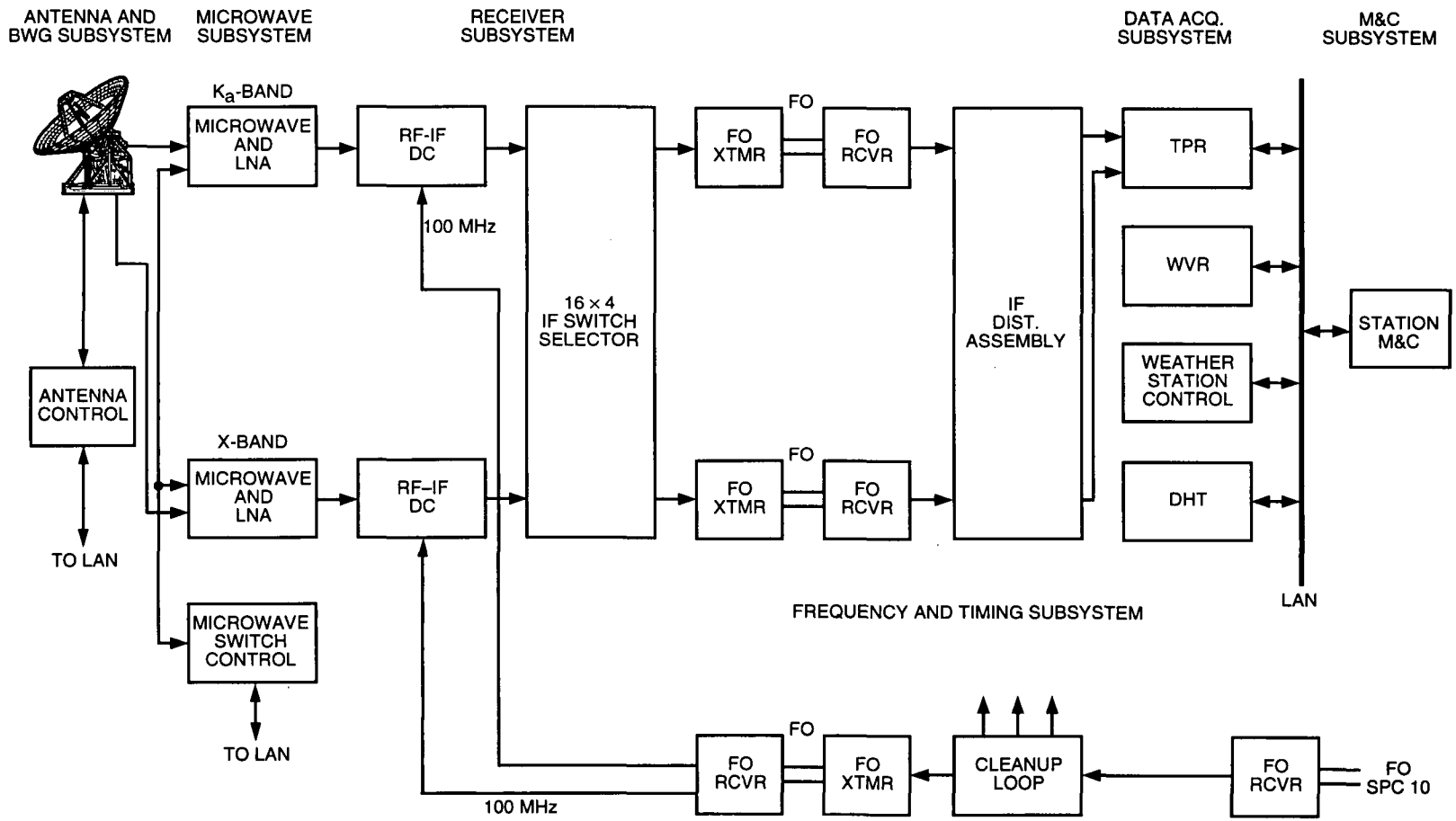

Fig. 3. The KaAP X-/Ka-band system at DSS-13.

to correct errors to about 5-mdeg rms in a blind or open-loop mode. Pointing errors were reduced by utilizing an improved automatic boresight technique, which corrects pointing errors in real time [5]. Since the tip-curve data involve cold sky observations, the pointing accuracy is not as critical as it is for the boresight observations used to estimate efficiency.

B. Microwave Subsystem

The microwave subsystem takes advantage of the pedestal room layout to allow switching between different feed packages arranged in a ring around a rotating ellipsoid reflector. The feed package used for KaAP consists of an X-/Ka-band dichroic plate, a 25-dBi horn for 8.4 GHz, a 26-dBi horn for 32 GHz, and high–electron mobility transistor (HEMT) low-noise amplifiers (LNAs) for both bands. The X-/Ka-band dichroic plate is essentially transparent at 32 GHz and reflective at 8.4 GHz. It was designed to study performance at the DSN-allocated 32.0-GHz frequency (to receive) and 34-GHz frequency (to transmit). However, because Mars Observer used a simple $\times 4$ to multiply its 8.4-GHz frequency up to 33.7 GHz, the downlink KaBLE 33.7-GHz frequency occurs at a nonoptimal location between two well-matched bands. Thus, the first data acquired for KaAP (December 93 to September 94) were at the 33.7-GHz frequency. With the installation of the new equipment designed to operate at the intended DSN-allocated 32.0-GHz frequency, the Ka-band data acquired since (October 94 to the present) have been at 32.0 GHz. The dichroic plate along with the added temperature of the HEMT contributes approximately 11 K of additional noise temperature at 33.7 GHz above that at 32 GHz. A description of the dichroic plate is found in [7].

For the LNA packages, HEMT devices were used at 8.4 and 32 GHz. The noise temperature contributions of 16.6 K (0.24 dB) by the 8.4-GHz feed in the low-noise path and 12 K by the 8.4-GHz LNA HEMT result in a contribution of 28.6 K for the full package.[1] This estimated value agrees well with a measured value of 28.4 K.[2] Temperature contributions of the follow-on equipment (downconverters, fiber-optic link) ranged from about 0.3 to 1.4 K.

The 32-GHz KaAP feed system includes a 26-dBi horn that is an extension to a 22-dBi corrugated horn, followed by a waveguide window at room temperature. An ellipsoidal reflector is located above the 32-GHz feed. The cool components include a round-to-square transition copper thermal isolator followed by a copper polarizer, a cross-guide coupler, a copper isolator, and a WR-28 copper waveguide going into the LNA. The KaAP 32-GHz LNA utilizes four stages of General Electric (GE) and Fujitsu transistors of basic National Radio Astronomy Observatory (NRAO) design, resulting in a total noise temperature of about 28 K. The cryogenic loss factor of the waveguide/feed package is estimated to be about 0.325 dB at both 32 and 33.7 GHz.[3] After adding room temperature contributions due to the window (0.02 dB) and the horn (0.04 dB), this results in an overall horn/waveguide/feed package loss of about 0.4 dB for a noise temperature contribution of about 5 K. The resulting estimated temperature of the total package (32 K) is somewhat lower but in reasonable agreement with 34- to 36-K values measured at the station in March 1994.[4]

For 32 GHz, an ambient load is swung over the horn for noise calibrations. For the 8.4-GHz system, a waveguide switch located in front of the LNA is used. Both ambient loads have embedded temperature sensors used in the calibration algorithms. Compressed helium gas is used to cool the LNA/waveguide feed package in closed-vessel systems. For the 32-GHz refrigerator system, there are four temperature sensors. For the 8.4-GHz system, there are two sensors.

---

[1] S. Stewart, personal communication, Jet Propulsion Laboratory, Pasadena, California, October 6, 1994.

[2] G. Bury, personal communication, Jet Propulsion Laboratory, Pasadena, California, October 4, 1994.

[3] J. Bowen, unpublished report (internal document), Jet Propulsion Laboratory, Pasadena, California, February 7, 1995.

[4] G. Bury and J. Garnica, personal communication, Jet Propulsion Laboratory, Pasadena, California, March–April 1994.

C. Receiver Subsystem

The receiver subsystem, used for both frequency bands, consists of RF-to-IF downconverters, a 16 × 4 IF switch selector, fiber-optic links from the pedestal room to the control room, and an IF distribution assembly in the control room. The 8.4-GHz downconversion is performed using a 8.1-GHz first local oscillator (LO). For the Ka-band path, two configurations have been used. During the 33.7-GHz data acquisition period (from December 1993 to October 1994), the incoming 33.7-GHz signal was mixed with a 25.2-GHz first LO followed by a 8.2-GHz second LO. The bandwidth of the second IF filter was 100 MHz. All LOs are coherent with the station frequency and timing subsystem (FTS). For the 32.0-GHz data acquisition, the incoming 32.0-GHz signal was mixed with a 23.6-GHz first LO followed by a 8.1-GHz second LO. The bandwidth of the second IF filter was 500 MHz. The downconverter outputs are amplified by IF amplifiers and fed into a 16 × 4 (16 input ports/4 output ports) switch selector, where two output signals, the 8.4-GHz and Ka-band IFs, are sent over fiber-optic links to the control room. The IFs are then input to an IF distribution assembly (amplifiers and power dividers) and ported to various subsystems in the control room.

D. Data Acquisition Subsystem

The instruments included in this subsystem include the total power radiometer (TPR) for measuring system noise temperature, the WVR for measuring the quantity of water in the atmosphere, the weather station, and the data handling terminal (DHT) for displaying data from other instruments and recording KaAP-specific data to disk.

The TPR operates together with the microwave switch controller (USC) to perform calibrated operating temperature, T_{op}, measurements during the track. The two IF channels are further filtered (usually 20 MHz for 8.4 GHz and 30 MHz for 32 GHz) to limit the noise coming in, such that radio frequency interference (RFI) can be minimized. The bandwidth of these filters together with the radiometer integration time and system gain stability define the contribution of the noise fluctuations of the temperature measurements. These filters together with a 5-s radiometer integration time constrain the random fluctuation contribution to below 0.01 K. Variable step attenuators are used to set the power levels to a 0.8- to 0.9-μW level when the antenna is on ambient load with the noise diode on. Measurements of the total IF noise power are made with two Hewlett Packard (HP)8481 power sensors followed by HP437 power meters—one each for 8.4 GHz and Ka-band. The power sensors operate from 10 MHz to 18 GHz and output 100-pW to 10-μW dc power levels. A local terminal reads these measurements and converts them to temperatures at a rate of 1 per second, based on a transfer function derived from a previous calibration.

Calibrations are performed alternately throughout the track with the boresight observations. During each calibration, the TPR measures the total IF noise power while the USC switches the HEMT input from (1) sky, to (2) sky plus noise diode, to (3) ambient load, and to (4) ambient load plus noise diode. The measurements are converted into a transfer function (T_{op} versus total noise power) and also allow for the estimation of system linearity.

The R6 WVR is a small stand-alone package positioned near the antenna that determines the presence of water in the atmosphere in vapor and droplet form (hydrometeors) along the antenna beams by measuring noise levels at 20.7 and 31.4 GHz over effective bandwidths of 320 MHz. It consists of a platform with a small feedhorn and mirror assembly that can observe any point in the sky with a beamwidth of 7 deg. It is located 300 m from the BWG antenna on the roof of the control building. A description of the R6 WVR is found in [8].

The WVR performs periodic tipping curves from zenith to 30-deg elevation and, when provided with pointing predicts, can track along the line of sight of the 34-m BWG antenna. The measured brightness temperatures have accuracies of about 0.5 K and precisions of about 0.1 K, based on intercomparisons with other WVRs.[5] During the KaAP data-acquisition period, the radiometer operates in a continuous

[5] S. Keihm, personal communication, Jet Propulsion Laboratory, Pasadena, California, May 5, 1995.

tip-curve mode, obtaining both gain calibration and zenith brightness temperature data with a 4.25-min sampling rate at both channels.

Data collected by the WVR are periodically delivered for correlation with the KaAP tipping-curve measurements. Both magnitudes and deviations of atmospheric temperatures between the two systems can be cross-compared. One expects better agreement between the BWG and WVR data on dry, clear days when the water vapor content is minimal. During inclement or cloudy conditions, the agreement is not expected to be as good. The results of the cross-comparison will be discussed in Section IV.A.2.

The weather system samples and records a range of meteorological parameters, including atmospheric pressure, air temperature, relative humidity, wind speed, and wind direction. The data are stored locally and routed through the station's monitor and control computer to a central storage device, the data handling terminal (DHT). The surface data can be input to a surface model, and the resulting atmospheric noise temperature at zenith can be cross-compared against those from the BWG tip curves and the WVR.

The DHT is routinely monitored for insight into the state of the data. Such data types are the operating temperature, elevation angle, and wind speed, which can be displayed simultaneously versus time on a single monitor. Most data arrive in the DHT through the station data recorder (SDR), a gateway terminal that serves to back up data archiving and relieve some of the real-time load from the DHT.

E. Monitor and Control Subsystem

Tying all of the systems together into an operational system with a high degree of flexibility is the monitor and control (M&C) subsystem. The main strength of the M&C is its user-friendly window-driven display system. As a step toward the goal of developing semiautomated monitor and control of operational procedures in the DSN, an operational prototype known as Link Monitor Control Operator Assist (LMCOA) was implemented at DSS 13. The LMCOA automation software was developed in a SUN/UNIX environment in C and RTworks. Originally targeted for automating KaBLE experiments, LMCOA was implemented for KaAP and has been used successfully for running KaAP experiments, including the tipping-curve data acquisition sequences. Several of the early data sets were acquired using an M&C system that ran on a 486 platform and one that ran on a SUN workstation (DEXTERITY), which is the current backup to LMCOA. Interfacing to the other subsystems is provided by the local area network (LAN). Each subsystem host computer taps into the LAN through a special board plugged into its chassis. A driver for handling real-time commands is loaded into the host computer's random-access memory (RAM) at power-up.

F. Frequency and Timing Subsystem

Fiber-optic technology is employed to provide all of the sensitive reference frequency distributions, including (1) the distribution of the reference first LO to the downconverters in the pedestal room and (2) the transmission of the broadband IF signals from the pedestal room to the control room. Optical fiber provides better stability than coaxial cable.

III. Model and Fit Scenario

KaAP data acquisition began in December 1993. The observation strategy and the model used to fit the tipping-curve data will be described in this section.

A. Description of Measurement Sequence

Tipping curves are performed at the start and/or end of a KaAP pass. The tipping-curve data-acquisition strategy involves taking a set of operating-temperature measurements at a series of different elevation angles (T_{op} versus θ), where θ goes from horizon to zenith or vice versa. Each elevation angle

corresponds to a specific number of air masses along the path. The operating temperature as a function of air mass typically has a signature as shown in Fig. 4 for the case of 32 GHz. Zenith system temperatures typically run at about 40 K at 8.4 GHz, 68 K at 33.7 GHz, and 57 K at 32.0 GHz. A tipping-curve sequence typically takes about 1/2 to 1 hour to perform. Normally, the atmosphere is sampled from 1 air mass (zenith) to about 4 air masses (14.5-deg elevation).

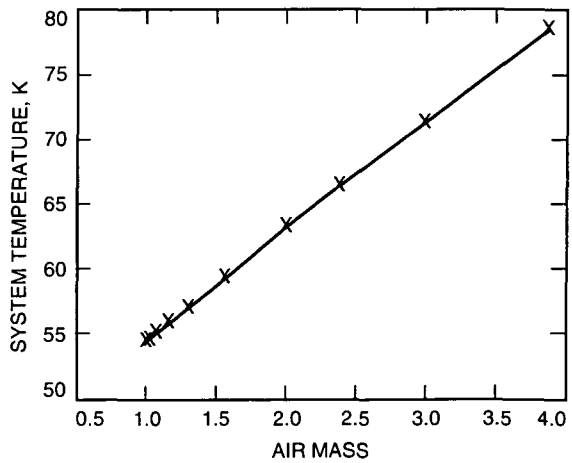

Fig. 4. Example of temperature versus air mass for a 32-GHz tip curve performed on 95-051.

From December 1993 to January 1994, the first series of KaAP experiments was performed. The tipping-curve data for this set of experiments utilized direct measurements from the TPR. However, these measurements were subject to uncalibrated gain changes during the tipping-curve measurement period. Beginning in February 1994, a new tipping-curve algorithm was employed at the DSS-13 BWG station that involved performing minicals in place of the regular radiometer temperature measurements. A minical employs an alternating sequence of the following temperature measurements: output device terminated (T_1), antenna on cold sky (T_2), antenna on cold sky plus noise diode (T_3), ambient load (T_4), and ambient load plus noise diode (T_5). The use of minicals calibrates gain variations as the tipping-curve data are acquired and allows for the determination of any small nonlinearity that may be in the system. The cold sky temperatures with the noise diode off (T_2) extracted from the minical output files are the observable data for the periods that these tipping curves were performed.

B. Description of Operating Temperature Model

The measured system operating noise temperature, T_{op}, is referenced at the input plane of the horn for 32 GHz, where an aperture load is swung above the horn during ambient temperature measurements, and at the input plane of the HEMT for 8.4 GHz, where a waveguide switch connects an ambient load during the measurements. T_{op} is expressed in terms of several contribution and loss factors that closely follow the formulation in [9], as given below:

$$T_{op} = \frac{(T^*_{cb}/L_{atm}) + T_{atm}}{L_{F1}L_{F3}L_{wg}} + \frac{T_{ant,F1}}{L_{F3}L_{wg}} + \frac{T_{ant,F3}}{L_{wg}} + T_{wg} + T_{lna} + T_f \tag{1}$$

where

T^*_{cb} = effective cosmic background temperature, K

T_{atm} = atmospheric noise temperature, K

L_{atm} = atmospheric loss factor

L_{F1} = Cassegrain reflector dissipative loss factor

L_{F3} = mirrors and dichroic plate dissipative loss factor

L_{wg} = loss factor due to components between feed horn and input flange of HEMT

$T_{ant,F1}$ = noise temperature due to spillover, leakage, and scattering of main reflector and subreflector, K

$T_{ant,F3}$ = noise temperature due to spillover, leakage, and scattering between F1 and F3, K

T_{wg} = noise temperature between the feed horn and input flange of HEMT, K

T_{lna} = temperature of the LNA, K

T_f = temperature contribution of follow-on electronics, K

Table 1 lists the current best-known values of several of these factors.

Table 1. Values of parameters used in Eq. (1).

Parameter	8.4 GHz	32.0 GHz	33.7 GHz
L_{F1}	1.011[a]	1.02[a]	1.02[a]
L_{F3}	1.0043[a]	1.01[a]	1.03[a]
L_{wg} (ambient)	1.057[b]	1.01742[c]	1.01742[c]
L_{wg} (cooled)	1.0[d]	1.078[e]	1.078[e]
T_{lna}	12.0[f]	28.0[f]	28.0[f]
T_f	0.3–0.9[g]	0.3–1.4[g]	0.3–1.4[g]

[a] Current best-known values.
[b] S. Stewart, op cit.
[c] R. Clauss, personal communication, Jet Propulsion Laboratory, Pasadena, California, February 22, 1995.
[d] Negligible cryogenic loss; assumed close to unity.
[e] J. Bowen, op cit.
[f] Baseline values inferred from lab measurements.
[g] Typical values routinely measured during prepass period.

The model typically used for the atmospheric noise temperature, T_{atm}, in the tipping-curve analysis assumes a stratified atmosphere that makes use of the equation of radiative transfer [10], which can be shown to reduce to a simplified exponential form. For the purpose of this analysis, we make use of a two-layer model of Kutner [11] in which the oxygen and water contributions to the opacity are treated separately. The atmospheric noise temperature, T_{atm}, and atmospheric loss factor, L_{atm}, thus assume elevation (air mass) dependent forms given by

$$T_{atm}(\theta) = T_{O_2}\left[1 - e^{-[\tau_{O_2}+\tau_{H_2O}]A(\theta)}\right] + [T_{H_2O} - T_{O_2}]\left[1 - e^{-\tau_{H_2O}A(\theta)}\right] \tag{2}$$

$$L_{atm}(\theta) = e^{(\tau_{O_2}+\tau_{H_2O})A(\theta)} \tag{3}$$

where

$A(\theta)$ = air mass number at elevation $\theta, \sim \sin^{-1}(\theta)$

T_{O_2} = radiating temperature of oxygen, K

T_{H_2O} = radiating temperature of water vapor and hydrometeors, K

τ_{O_2} = opacity of oxygen contribution

τ_{H_2O} = opacity of water contribution

Prior to performing a fit, all known contributions due to equipment (HEMT and follow-on), waveguide, and antenna losses (spillover, scatter, and leakage) are removed from T_{op} in Eq. (1) as follows:

$$\Delta T^*_{op} = T_{op} - \frac{T_{ant}(\theta)}{L_{F3}L_{wg}} - T_{wg} - T_{lna} - T_f \tag{4}$$

The contributions remaining in the residual temperature of Eq. (4) include the cosmic and atmospheric noise temperature contributions. Since the cosmic term includes a dependence on the atmospheric loss factor, it is retained in the residual data prior to the fit. Each contributing quantity removed prior to fitting a model is discussed below.

1. Antenna Temperature Contribution. In order to simplify the analysis, we consider that most of the elevation-dependent signature in the antenna temperature is due to the tripod scatter and main reflector dissipative losses in the $T_{ant,F1}$ term. We assume that the elevation-dependent signature in the mirrors, $T_{ant,F3}$ in Eq. (1), is small and, thus, effectively a constant and, therefore, lumped with $T_{ant,F1}$ in the T_{ant} term in Eq. (4). The antenna noise temperature, T_{ant}, is removed from the data as shown in Eq. (4) for 8.4 and 32.0 GHz prior to performing the fit. It is the sum of contributions due to spillover, mirror/gap losses, and tripod scatter, and is a known function of elevation angle. Veruttipong provides values of the antenna noise temperature, $T_{ant}(\theta)$, at three elevation angles, 10, 30, and 90 deg, for both 8.4 and 32 GHz.[6] A quadratic form for $T_{ant}(\theta)$ was used and coefficients derived from the "predicted" values of Veruttipong at the three elevation angles as defined by

$$T_{ant}(\theta) = C_1 + C_2(90 - \theta) + C_3(90 - \theta)^2 \tag{5}$$

where θ is the elevation angle in deg.

For 32 GHz, the coefficients inferred from Eq. (5) using Veruttipong's data are $C_1 = 9.25$ K, $C_2 = 0.00020835$ K/deg, and $C_3 = 0.0002278$ K/deg^2. At 33.7 GHz, a constant 11 K is added to the bias term (C_1) to account for additional loss contributions (e.g., dichroic) at this frequency.

While the Veruttipong results imply that the antenna noise temperature dependence with elevation angle, $T_{ant}(\theta)$, is essentially the same for both 8.4 GHz and Ka bands, attempts to use the three (similarly derived) coefficients at 8.4 GHz resulted in unreasonable estimates. The predicted values may have been derived under assumptions that do not apply for DSS 13's tripod structure and forward and rear spillover differences between 8.4- and 32-GHz frequencies.

The coefficients for 8.4 GHz were derived by first assuming a constant term (C_1) and setting the other terms to zero ($C_2 = C_3 = 0$). For this analysis, the elevation-dependent signature of the atmosphere

[6] W. Veruttipong, "Detailed Gain/Noise Budgets at X- and Ka-Bands for KABLE Experiment," JPL Interoffice Memorandum 3328-92-0190 (internal document), Jet Propulsion Laboratory, Pasadena, California, December 29, 1992.

is assumed to be uncoupled to that of the antenna. The data were processed for a select subset of dry weather passes. The resulting postfit residuals had repeated signatures with a significant 0.2-K change over elevation angle, consistent with the quoted 0.2-K uncertainty of earlier work at 8.4 GHz [12], where an elevation-dependent antenna temperature model was also not employed. The authors of [12] attributed the 0.2-K level of agreement to the low amount of scattering due to the slim tripod legs of the BWG antenna. The signature of the postfit residuals appeared remarkably repeatable between data sets. The second-degree polynomial model [Eq. (5)] was then fit to these postfit signatures. The average values of C_1, C_2, and C_3 derived from the dry weather subset of tip curves were used for the antenna temperature model of Eq. (5) at 8.4 GHz. This model was fed back in Eq. (4), resulting in lower rms scatters in the postfit residuals and negligible remaining systematic signatures. The derived 8.4-GHz coefficients used for T_{ant} in Eq. (5) were $C_1 = 7.0$ K, $C_2 = -0.0087$ K/deg, and $C_3 = 0.000110$ K/deg^2. Figure 5 displays the 8.4- and 32.0-GHz antenna temperature versus elevation angle models [Eq. (5)] that were removed from the data [Eq. (4)] prior to performing the fit.

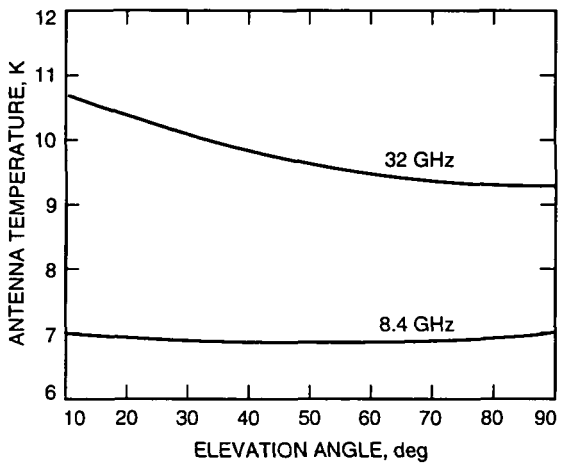

Fig. 5. The 8.4- and 32-GHz antenna temperature model versus elevation angle.

2. Ambient Feed Component Contributions. The waveguide noise temperature contribution, T_{wg}, of the horn, window, and other components at ambient is computed from the loss factor, L_{wg}, and physical temperature, T_p, as follows:

$$T_{wg} = \left[1 - \frac{1}{L_{wg}}\right] T_p$$

In practice, T_{wg} cannot be measured unless the waveguide/feed package is physically removed from the LNA. The combined waveguide/LNA temperature can be measured during cold load/warm load measurements performed during maintenance periods and compared against preinstallation measurements (or predictions) of the LNA and waveguide/feed package temperatures. The current best-known values of the ambient waveguide package loss factors are $L_{wg}(X) = 1.057$ (0.24 dB),[7] and $L_{wg}(K_a) = 1.01742$ (0.075 dB).[8]

3. Cryogenically Cooled Component Contributions. The noise temperature contributions of cryogenically cooled components in front of the LNA are assumed embedded in the T_{lna} baseline values. Baseline values of the temperatures of the cooled components, T_{lna} (LNA and waveguide), are removed from the measurements (12 K for 8.4 GHz and 28 K for Ka-band). If all other contributors have been

[7] S. Stewart, op cit.

[8] R. Clauss, personal communication, Jet Propulsion Laboratory, Pasadena, California, February 22, 1995.

accurately removed, then we expect the variation of any bias terms fit from the data will reflect the variation of the temperature of these components. The results will be discussed in a later section.

4. Follow-On Equipment Contribution. The follow-on equipment (T_f) noise temperature contributions are routinely measured prior to each pass and are removed from the observed temperatures as given in Eq. (4). Typical values of T_f range from about 0.3 to 1.4 K and depend upon the state and configuration of the equipment for a particular pass. For a few of the earlier passes, a significant 1.4-K follow-on measurement at 32 GHz was attributed to faulty equipment.

C. Description of Fitting Algorithm

1. Nominal Two-Parameter Fits. After removing all known contributions from the data with the model in Eq. (4), the residual data are fit to provide the unmodeled bias and the cosmic and atmospheric contributions. The bias or constant term should indicate how well the model agrees with the measurements at zenith and how it varies from tip curve to tip curve or pass to pass. The elevation-dependent signature of the remaining contributions allows the atmospheric noise temperature contribution at zenith to be determined. By rearranging and combining terms in Eq. (4) using Eqs. (1) through (3), the model used to fit the data ΔT^*_{op} versus θ is given by

$$\Delta T^*_{op}(\theta) = T_{off} + \frac{(T^*_{cb}/[L_{atm}(\theta)]) + T_{atm}(\theta)}{L_{ant}} \tag{6}$$

where

$$L_{ant} = L_{F1} L_{F3} L_{wg}$$

From the residual temperatures in Eq. (6) for each tip-curve data set, a two-parameter model fit is performed, yielding the bias, T_{off}, and the opacity of water, τ_{H_2O}, which appears in Eq. (6) in the term T_{atm}, as shown in Eq. (2). Constant values are used for all other terms. The opacity of atmospheric oxygen (τ_{O_2}) used in Eq. (2) is estimated from the surface data using the SDSATM4S program.[9] The radiating temperature of water, T_{H_2O}, is computed from the surface temperature, T_0, as $T_{H_2O} = T_0 - 10$ K. The radiating temperature of oxygen, T_{O_2}, is taken to be 265 K. The effective cosmic background temperature (T^*_{cb}) assumed for 8.4 GHz is 2.5 K, and for 32 GHz it is 2.0 K.

2. Special Case Three-Parameter Fits. Significantly higher than usual postfit rms scatters for some of the earlier data sets conducted between 93-336 (December 2, 1993) and 94-024 (January 24, 1994) were attributed to linear drifts in temperature over the tip-curve measurement period. These passes did not employ minicals (which calibrate gain variations) during the tip-curve measurement sequences. During this period, the few cases of observed high-temperature gradients significantly skewed the fit results. A three-parameter model was employed to process these data sets. This model included the solve-for terms T_{off} and τ_{H_2O} as before in Eq. (6) and an additional term, $R(t - t_0)$, where R, the linear drift rate in K/h, is the additional solve-for parameter, t is the time tag of the data point, and t_0 is the reference time tag. For all passes conducted since 94-053 (February 22, 1994), minicals were performed for the tipping curves in place of the regular radiometer measurements, and these were processed as described in Section III.C.1 above.

IV. Results

A. Model Fit Results

A total of 67 Ka-band (33.7- and 32.0-GHz) and 68 X-band (8.425-GHz) tipping-curve data sets from the KaAP experiments conducted between 93-336 (December 2, 1993) and 95-137 (May 17, 1995) were

[9] Courtesy of S. Slobin, Jet Propulsion Laboratory, Pasadena, California, program version dated February 8, 1993.

processed with the KaAP tipping-curve analysis software. The Ka-band data acquired prior to and up to 94-270 were at 33.7 GHz, and data acquired since were at 32.0 GHz.

Two-parameter or three-parameter fits of each tip-curve data set using Eq. (6) were performed solving for the offset temperature, T_{off} (which is a measure of any remaining bias not accounted for in the model), and the opacity of water, τ_{H_2O} (which provides information on the atmosphere). The atmospheric temperature at zenith, T_{atm} (90 deg), is computed from τ_{H_2O} and other terms using

$$T_{atm}(90 \text{ deg}) = T_{O_2}\left[1 - e^{-(\tau_{H_2O}+\tau_{O_2})}\right] + [T_{H_2O} - T_{O_2}]\left[1 - e^{-\tau_{H_2O}}\right] \tag{7}$$

After fitting and removing the fitted model from the data, the postfit residuals can be inspected against time and air mass. The resulting residuals have time-dependent signatures, as shown in Fig. 6 for the 32-GHz data of Fig. 4.

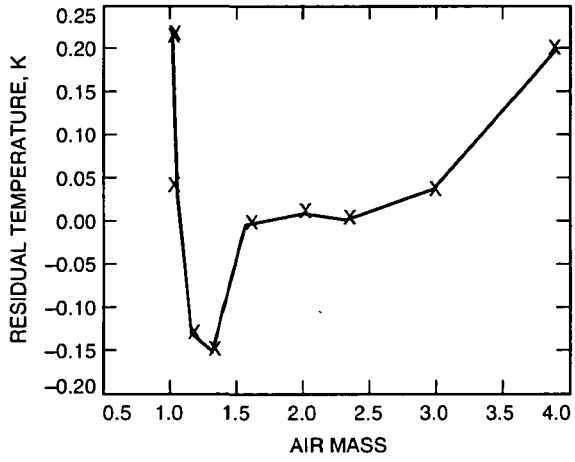

Fig. 6. Temperature residuals of tip-curve data of Fig. 4 after removing the fit model. Data from one to three air masses were fit.

Although data were routinely acquired from one air mass (zenith) to four air masses (14.5 deg), only the data from zenith to three air masses (19.5 deg) were fit in order to reduce the effect of unmodeled ground pickup and scatter at the lower elevations. Tables 2 and 3 display the results of the fit from the data sets for Ka-band and 8.4 GHz, respectively.

1. Bias Term of Solution. Figures 7 and 8 display the bias temperatures at zenith resulting from the fits of all of the tipping-curve data sets listed in Table 2 (32 GHz) and Table 3 (8.4 GHz), respectively. The few-K agreement with the baseline zenith model (zero) is reasonable given that they are correlated with known logged temperatures of the HEMT refrigeration units. Higher than usual temperature variations appear to be correlated with the state of the refrigeration units as they degrade over time prior to servicing, and the lower values are correlated with periods right after the units have been serviced. For instance, drops in observed bias temperatures, such as the 2.4-K drop on day 482 (94-117) for the 32-GHz case (Fig. 7), agree with drops of the refrigerator temperatures observed from the refrigeration servicing logs. Other differences of the bias term from the baseline may be attributed to uncertainties in the antenna-elevation model terms at zenith, such as the dissipative temperatures being different before and after periods of mirror or subreflector alignments or fluctuations of the atmosphere during the tipping-curve data acquisition period manifesting themselves into the bias term.

Table 2. The 32-GHz tipping-curve fit results.

Year	DOY	UTC Time		Zenith bias temperature, K	Atmosphere temperature, K	RMS, K	Notes
		Start	End				
93	336	15:52	15:59	5.84 ± 0.08	10.940 ± 0.064	0.133	
93	354	16:01	16:45	6.12 ± 0.06	9.689 ± 0.040	0.243	
93	354	22:37	22:55	5.81 ± 0.04	8.924 ± 0.027	0.104	
93	361	16:42	17:02	4.83 ± 0.18	12.791 ± 0.132	0.611	
93	361	22:13	22:33	5.42 ± 0.06	11.971 ± 0.049	0.209	
94	10	16:02	16:41	4.74 ± 0.04	9.700 ± 0.030	0.190	
94	17	15:57	16:25	5.65 ± 0.05	10.504 ± 0.040	0.227	
94	17	22:30	22:47	5.62 ± 0.03	11.025 ± 0.022	0.085	
94	24	16:16	16:45	7.58 ± 0.37	9.687 ± 0.282	1.199	
94	53	00:11	00:38	6.07 ± 0.17	9.760 ± 0.138	0.112	
94	59	15:42	17:00	6.50 ± 0.13	10.927 ± 0.101	0.100	
94	67	09:21	10:06	6.25 ± 0.16	11.050 ± 0.130	0.099	
94	73	13:46	14:37	9.81 ± 0.22	9.811 ± 0.181	0.141	
94	73	23:02	23:45	6.51 ± 0.15	10.322 ± 0.142	0.103	
94	80	22:38	23:01	2.35 ± 0.76	11.831 ± 0.624	0.185	
94	115	15:27	16:04	9.26 ± 0.32	10.280 ± 0.258	0.209	
94	122	15:05	16:02	2.94 ± 0.07	12.342 ± 0.055	0.033	
94	122	21:44	22:42	2.49 ± 0.28	12.846 ± 0.265	0.195	
94	123	22:55	23:44	3.37 ± 0.23	13.154 ± 0.213	0.145	
94	124	05:11	06:01	3.46 ± 0.07	13.573 ± 0.057	0.033	
94	129	08:31	08:58	3.17 ± 0.26	13.685 ± 0.201	0.061	
94	136	14:44	15:26	3.31 ± 0.39	10.718 ± 0.324	0.147	
94	137	22:44	23:10	3.18 ± 0.57	11.305 ± 0.489	0.212	
94	143	15:07	15:53	3.55 ± 0.25	9.972 ± 0.232	0.114	
94	158	15:10	16:08	3.44 ± 0.17	10.420 ± 0.134	0.082	
94	158	21:29	22:03	3.38 ± 0.27	11.179 ± 0.251	0.100	
94	160	23:14	23:42	3.00 ± 0.06	10.001 ± 0.057	0.016	
94	166	18:52	19:19	2.90 ± 0.45	10.539 ± 0.386	0.111	
94	172	22:38	23:07	3.13 ± 0.64	13.729 ± 0.642	0.237	
94	178	22:49	23:12	2.68 ± 0.68	16.667 ± 0.668	0.161	Cloudy
94	192	14:58	15:23	4.49 ± 0.34	8.854 ± 0.314	0.129	
94	199	15:20	15:38	2.37 ± 1.62	20.161 ± 1.606	0.574	Cloudy
94	206	15:41	16:05	2.91 ± 0.05	11.839 ± 0.036	0.025	
94	220	15:01	15:25	3.79 ± 0.27	17.373 ± 0.264	0.098	
94	229	23:19	23:39	4.05 ± 0.38	22.111 ± 0.316	0.233	Cloudy
94	255	22:44	23:07	2.97 ± 0.51	10.646 ± 0.364	0.335	
94	265	22:46	23:16	3.74 ± 0.15	14.304 ± 0.117	0.096	
94	269	15:25	15:51	3.10 ± 0.20	14.433 ± 0.158	0.142	Cloudy
94	270	05:23	05:48	4.19 ± 0.15	12.419 ± 0.110	0.097	Cloudy
94	283	14:57	15:20	1.30 ± 0.20	10.292 ± 0.140	0.132	
94	284	05:31	05:53	1.79 ± 0.16	10.918 ± 0.116	0.107	
94	286	14:52	15:13	1.32 ± 0.16	10.583 ± 0.102	0.103	

Table 2. The 32-GHz tipping-curve fit results (continued).

Year	DOY	UTC Time		Zenith bias temperature, K	Atmosphere temperature, K	RMS, K	Notes
		Start	End				
94	286	18:47	19:08	1.48 ± 0.17	11.009 ± 0.113	0.108	
94	297	16:02	16:25	2.09 ± 0.25	14.149 ± 0.177	0.160	
94	298	05:53	06:15	1.58 ± 0.14	13.942 ± 0.098	0.089	
94	306	16:01	16:23	−0.73 ± 0.82	16.310 ± 0.706	0.298	Windy
94	311	18:25	18:48	1.72 ± 0.41	9.258 ± 0.271	0.271	
94	325	18:52	19:15	1.50 ± 0.20	8.721 ± 0.125	0.130	
94	340	07:15	07:40	7.71 ± 2.07	9.449 ± 1.318	1.367	
95	3	07:08	07:31	9.43 ± 0.81	11.462 ± 0.511	0.531	Rainy
95	6	16:35	16:59	3.93 ± 1.07	16.517 ± 0.706	0.676	Rainy
95	9	23:13	23:33	2.65 ± 0.36	13.074 ± 0.242	0.232	Rainy
95	23	16:53	17:12	8.18 ± 1.27	21.557 ± 0.861	0.794	Rainy
95	23	17:34	18:11	24.83 ± 4.45	12.448 ± 3.060	3.938	Rainy
95	37	19:22	19:46	1.90 ± 0.15	8.641 ± 0.106	0.103	
95	38	04:53	05:43	1.82 ± 0.13	10.258 ± 0.085	0.132	
95	51	02:32	03:12	1.66 ± 0.13	9.524 ± 0.088	0.108	
95	51	20:05	20:46	1.76 ± 0.11	9.752 ± 0.084	0.106	
95	66	15:13	15:36	1.77 ± 0.16	8.129 ± 0.102	0.107	
95	81	14:40	15:28	2.76 ± 0.10	8.565 ± 0.061	0.110	
95	95	00:23	01:56	2.80 ± 0.18	8.946 ± 0.132	0.122	
95	109	13:16	14:04	3.85 ± 0.17	10.470 ± 0.103	0.178	
95	117	19:28	14:08	3.29 ± 0.33	12.299 ± 0.253	0.820	
95	122	11:36	11:55	3.68 ± 0.15	11.184 ± 0.110	0.101	
95	125	22:02	22:19	3.00 ± 0.24	10.493 ± 0.161	0.158	
95	128	15:28	15:45	3.91 ± 0.21	12.129 ± 0.140	0.137	
95	137	17:46	19:47	4.77 ± 0.17	12.047 ± 0.113	0.083	
Averages				4.18 ± 3.33	11.845 ± 2.898	0.277	

Figures 9 and 10 display the zenith temperatures for each tip-curve data set at 32 and 8.4 GHz, respectively. The large drop of about 11 K around day 650 on the 32-GHz plot (Fig. 9) occurs after the system was modified from 33.7 to 32.0 GHz.

During passes when the weather was rainy, the model breaks down, as seen for tip curves conducted in January 1995. During these tip-curve periods, the large variability in the atmospheric noise temperature introduces signatures that couple into the bias term. This effect is significant at 32 GHz (see passes 95-003 through 95-023 in Table 2 and days 733 through 753 in Fig. 9).

2. Atmospheric Noise Temperature Term of Solution. Figures 11 and 12 display the T_{atm} estimated from the fits for each tipping-curve data set listed in Tables 2 (32 GHz) and 3 (8.4 GHz), respectively. The 32-GHz values range from 8.1 to 22 K with typical rms scatters of about 0.1 K. The excessively large rms scatter of 4 K for pass 95-023 is illustrative of the case of very stormy weather conditions, discussed previously in Section IV.A.1. The 8.4-GHz atmosphere temperatures range from 2.0 to 3.9 K with typical rms scatters of about 0.03 K with values as high as 0.7 K. Atmospheric fluctuations

Table 3. The 8.4-GHz tipping-curve fit results.

Year	DOY	UTC Time		Zenith bias temperature, K	Atmosphere temperature, K	RMS, K	Notes
		Start	End				
93	336	15:52	15:59	0.84 ± 0.02	2.263 ± 0.018	0.042	
93	354	16:01	16:45	1.19 ± 0.03	2.186 ± 0.018	0.125	
93	354	22:37	22:55	1.34 ± 0.01	2.289 ± 0.009	0.040	
93	361	16:42	17:02	1.02 ± 0.04	2.389 ± 0.024	0.130	
93	361	22:13	22:33	1.72 ± 0.02	2.330 ± 0.013	0.066	
94	10	16:02	16:41	0.71 ± 0.02	2.216 ± 0.011	0.080	
94	17	15:57	16:25	1.19 ± 0.02	2.239 ± 0.012	0.080	
94	17	22:30	22:47	1.12 ± 0.02	2.239 ± 0.013	0.059	
94	24	16:16	16:45	1.32 ± 0.02	2.249 ± 0.017	0.078	
94	67	09:20	10:05	0.33 ± 0.04	2.296 ± 0.037	0.029	
94	73	13:45	14:36	−0.02 ± 0.04	2.264 ± 0.034	0.027	
94	73	22:59	23:40	0.32 ± 0.14	1.985 ± 0.127	0.087	
94	80	22:33	23:00	−0.22 ± 0.01	2.326 ± 0.010	0.003	
94	87	16:00	16:25	0.18 ± 0.08	2.294 ± 0.069	0.054	
94	87	22:07	22:35	0.07 ± 0.02	2.280 ± 0.018	0.014	
94	94	14:49	21:54	1.18 ± 0.06	2.279 ± 0.049	0.052	
94	101	15:07	15:32	1.44 ± 0.20	2.904 ± 0.145	0.244	
94	122	15:03	16:01	1.49 ± 0.05	2.431 ± 0.042	0.026	
94	122	21:42	22:41	1.46 ± 0.06	2.338 ± 0.061	0.047	
94	123	22:53	23:43	1.14 ± 0.05	2.469 ± 0.049	0.035	
94	124	05:09	06:00	1.91 ± 0.03	2.467 ± 0.026	0.016	
94	129	08:29	08:56	1.68 ± 0.04	2.473 ± 0.033	0.011	
94	136	14:58	15:25	1.23 ± 0.11	2.565 ± 0.093	0.038	
94	137	22:42	23:08	1.35 ± 0.14	2.316 ± 0.119	0.053	
94	143	15:05	15:51	0.92 ± 0.02	2.284 ± 0.022	0.011	
94	158	15:08	16:07	1.10 ± 0.03	2.242 ± 0.026	0.017	
94	158	21:27	22:03	0.67 ± 0.04	2.340 ± 0.033	0.014	
94	160	23:12	23:40	0.47 ± 0.01	2.164 ± 0.013	0.006	
94	166	18:51	19:18	0.86 ± 0.13	2.109 ± 0.115	0.034	
94	172	22:37	23:06	0.35 ± 0.07	2.448 ± 0.072	0.029	
94	178	22:43	23:11	0.30 ± 0.06	2.700 ± 0.058	0.016	Cloudy
94	192	14:56	15:22	0.66 ± 0.05	2.172 ± 0.050	0.021	
94	199	15:18	15:33	0.63 ± 0.16	2.905 ± 0.159	0.065	Cloudy
94	206	15:39	16:04	−0.41 ± 0.11	2.356 ± 0.075	0.057	
94	220	14:59	15:24	−0.59 ± 0.01	2.796 ± 0.011	0.012	
94	229	23:18	23:37	−1.08 ± 0.14	3.154 ± 0.105	0.096	Cloudy
94	255	22:42	23:05	−0.90 ± 0.08	2.354± 0.059	0.057	
94	265	22:44	23:14	−0.96 ± 0.06	2.683 ± 0.043	0.040	
94	269	15:23	15:49	−0.80 ± 0.07	2.674 ± 0.054	0.054	Cloudy
94	270	05:26	05:47	−0.79 ± 0.12	2.528 ± 0.086	0.082	Cloudy
94	283	14:55	15:18	0.00 ± 1.45	3.903 ± 1.198	0.717	
94	284	05:29	05:52	1.26 ± 0.05	2.620 ± 0.035	0.034	

Table 3. The 8.4-GHz tipping-curve fit results (continued).

Year	DOY	UTC Time		Zenith bias temperature, K	Atmosphere temperature, K	RMS, K	Notes
		Start	End				
94	286	14:50	15:11	1.78 ± 0.08	2.571 ± 0.054	0.059	
94	286	18:45	19:06	1.39 ± 0.73	2.587 ± 0.472	0.466	
94	297	16:00	16:23	−0.57 ± 0.06	2.679 ± 0.041	0.041	
94	298	05:51	06:13	−0.81 ± 0.07	2.699 ± 0.052	0.052	
94	306	15:59	16:21	−0.44 ± 0.17	2.887 ± 0.113	0.119	Windy
94	311	18:24	18:46	0.04 ± 0.04	2.358 ± 0.023	0.024	
94	325	18:50	19:14	0.40 ± 0.04	2.386± 0.029	0.031	
94	340	07:14	07:38	0.74 ± 0.10	2.406 ± 0.067	0.071	
95	3	07:06	07:29	0.62 ± 0.13	2.571 ± 0.084	0.093	Rainy
95	6	16:34	16:58	0.68 ± 0.41	3.046 ± 0.255	0.281	Rainy
95	9	23:12	23:32	0.44 ± 0.17	2.580 ± 0.113	0.119	Rainy
95	23	16:51	17:14	0.29 ± 0.25	3.724 ± 0.154	0.178	Rainy
95	23	17:32	18:10	0.76 ± 0.74	3.596 ± 0.509	0.701	Rainy
95	37	19:20	19:44	−0.12 ± 0.10	2.353 ± 0.072	0.072	
95	38	04:51	05:41	0.12 ± 0.04	2.468 ± 0.029	0.047	
95	51	02:31	03:10	0.14 ± 0.07	2.335 ± 0.046	0.058	
95	51	20:04	20:45	0.07 ± 0.07	2.331 ± 0.056	0.074	
95	66	15:11	15:34	0.46 ± 0.08	2.254 ± 0.052	0.055	
95	81	14:38	15:27	0.59 ± 0.07	2.278 ± 0.040	0.074	
95	95	01:31	01:50	0.00 ± 0.09	2.289 ± 0.065	0.063	
95	109	13:14	14:02	0.82 ± 0.06	2.368 ± 0.035	0.063	
95	117	13:46	14:07	0.93 ± 0.09	2.357 ± 0.054	0.060	
95	122	11:34	11:53	0.10 ± 0.06	2.376 ± 0.045	0.044	
95	125	22:01	22:15	0.51 ± 0.13	2.443 ± 0.081	0.068	
95	128	15:26	15:43	0.70 ± 0.06	2.490 ± 0.040	0.043	
95	137	17:46	19:46	0.59 ± 0.22	2.379 ± 0.142	0.114	
Averages				0.53 ± 0.73	2.490 ± 0.350	0.086	

over the time scale of the tip-curve period are assumed to be the dominating contributor to the rms scatters for most of the data sets, where the rms scatter exceeds the expected 0.04-K gain fluctuations.

Tables 4 and 5 display the BWG, WVR, and surface model (SURF)-derived atmospheric noise temperatures at zenith for 32- and 8.4-GHz, respectively, for a select subset of data sets. Also provided are the difference temperatures BWG–WVR and BWG–SURF. The differences of the tip-curve values with those derived from the WVR data for this select subset are displayed in Figs. 13 and 14 for 32 and 8.4 GHz, respectively.

The 32- or 33.7-GHz WVR-derived values were computed by (1) fitting a straight line over the 31.4-GHz zenith WVR data across the BWG tip-curve interval, (2) taking the linear fit value at the midpoint of the interval, (3) removing the effective cosmic contribution for 32 GHz, and (4) then correcting the WVR value to the frequency of the tip-curve data by adding 0.2 K to refer to 32 GHz and 0.95 K for 33.7 GHz. The 8.4-GHz WVR-derived values were computed from the 31.4-GHz zenith WVR data as

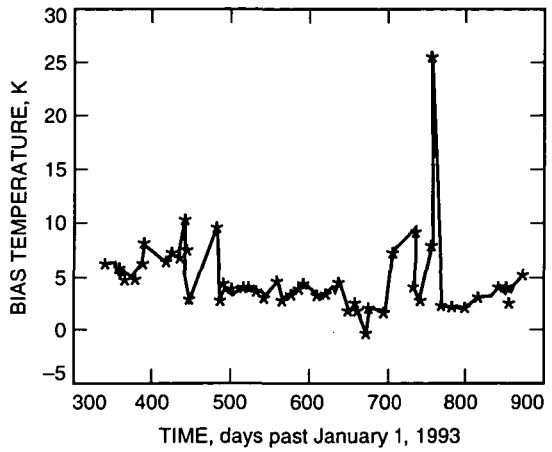

Fig. 7. Bias temperatures at 32 GHz.

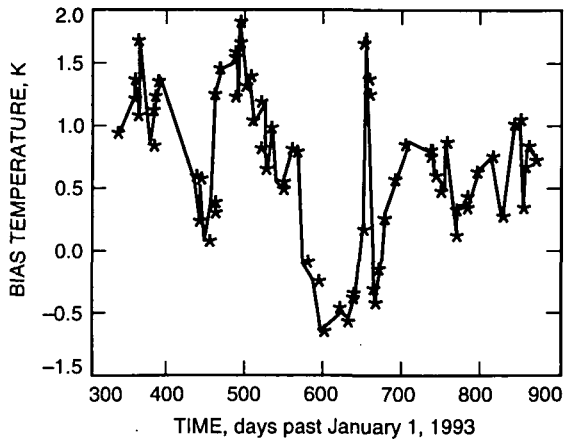

Fig. 8. Bias temperatures at 8.4 GHz.

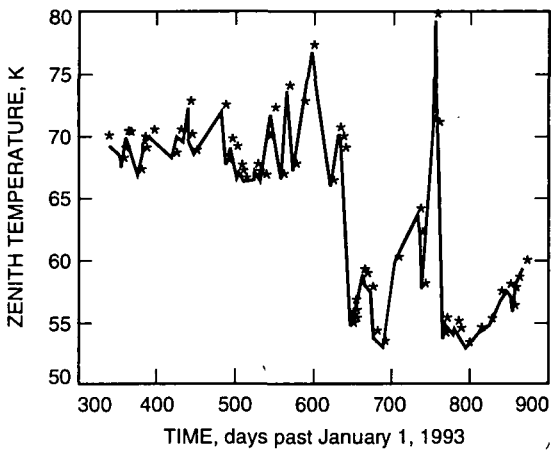

Fig. 9. Zenith temperatures at 32 GHz over the tip-curve period.

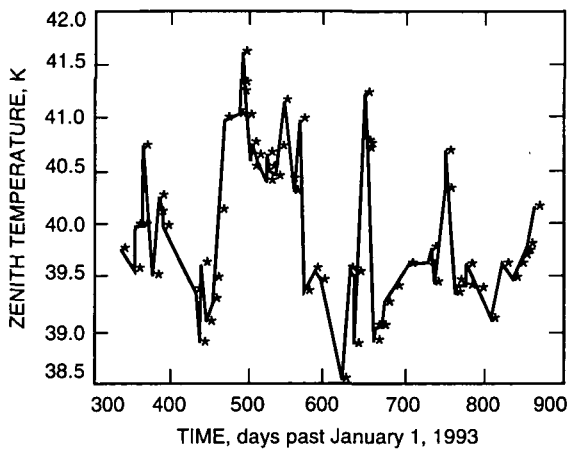

Fig. 10. Zenith temperatures at 8.4 GHz over the tip-curve period.

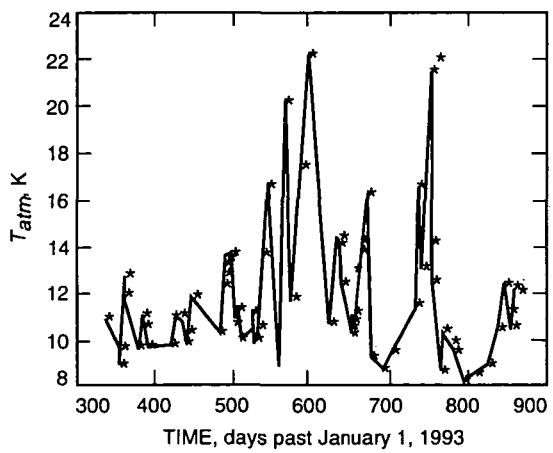

Fig. 11. Atmospheric noise temperatures at zenith for 32 GHz from fit of tip-curve data.

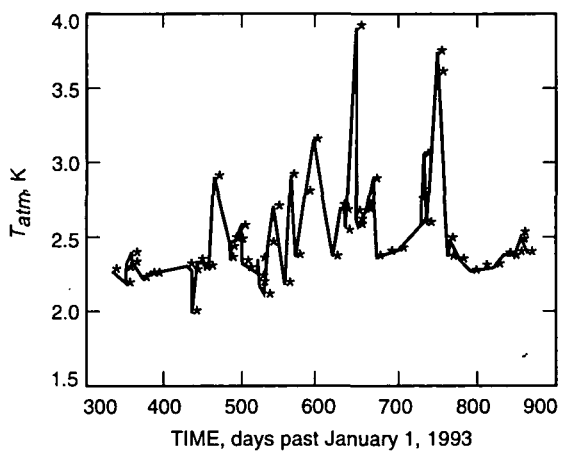

Fig. 12. Atmospheric noise temperatures at zenith for 8.4 GHz from fit of tip-curve data.

Table 4. The 32-GHz BWG, WVR, and surface model (SURF)-derived zenith atmospheric noise temperatures and scatters.

Year	DOY	UTC Time		T_{BWG}, K	RMS	T_{WVR}, K	RMS	T_{SURF}, K	$T_{BWG} - T_{WVR}$, K	$T_{BWG} - T_{SURF}$, K
		Start	End							
94	17	15:57	16:25	10.504	0.227	10.420	0.159	6.994	0.084	3.510
94	17	22:30	22:47	11.025	0.085	10.745	0.131	7.154	0.280	3.871
94	24	16:16	16:45	9.687	1.199	9.911	0.130	11.285	−0.224	−1.598
94	115	15:27	16:04	10.280	0.209	11.208	0.117	9.168	−0.928	1.112
94	122	15:05	16:02	12.342	0.033	12.511	0.114	10.779	−0.169	1.563
94	122	21:44	22:42	12.846	0.195	12.326	0.413	8.483	0.520	4.363
94	123	22:55	23:44	13.154	0.145	13.633	0.158	8.731	−0.479	4.423
94	124	05:11	06:01	13.573	0.033	13.951	0.137	11.051	−0.378	2.522
94	158	15:10	16:08	10.420	0.082	10.554	0.170	9.715	−0.134	0.705
94	158	21:29	22:03	11.179	0.100	11.895	0.100	8.493	−0.716	2.686
94	178	22:49	23:12	16.667	0.161	16.142	0.297	10.384	0.525	6.283
94	199	15:20	15:38	20.161	0.574	18.341	0.130	11.259	1.820	8.902
94	220	15:01	15:25	17.373	0.098	17.282	0.093	10.010	0.091	7.363
94	229	23:19	23:39	22.111	0.233	22.293	0.200	16.984	−0.182	5.127
94	255	22:44	23:07	10.646	0.335	10.617	0.376	9.329	0.029	1.317
94	297	16:02	16:25	14.149	0.160	14.287	0.194	8.141	−0.138	6.008
94	298	05:53	06:15	13.942	0.089	13.214	0.262	10.848	0.728	3.094
94	306	16:01	16:23	16.310	0.298	15.142	0.647	11.137	1.168	5.173
94	311	18:25	18:48	9.258	0.271	9.463	0.202	6.646	−0.205	2.612
94	325	18:52	19:15	8.721	0.130	9.122	0.062	5.980	−0.401	2.741

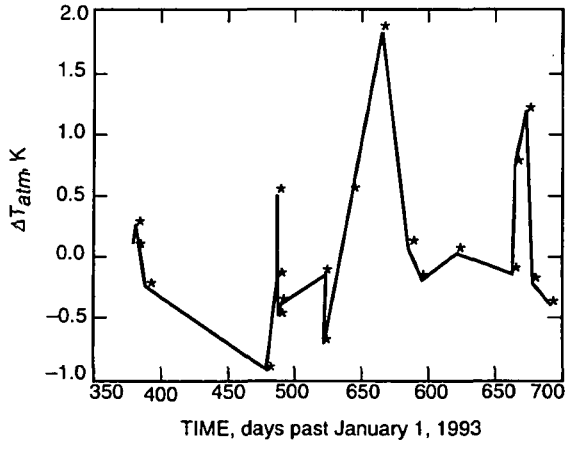

Fig. 13. Differences of 32-GHz tip curve T_{atm} from those estimated from 31.4-GHz WVR zenith data.

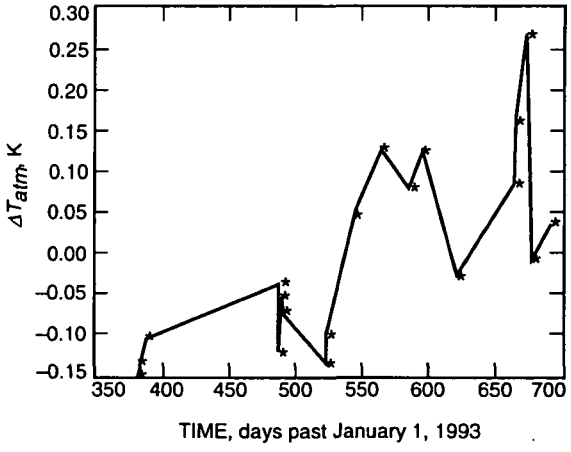

Fig. 14. Differences of 8.4-GHz tip curve T_{atm} from those estimated from 31.4-GHz WVR zenith data.

Table 5. The 8.4-GHz BWG, WVR, and surface model (SURF)-derived zenith atmospheric noise temperatures and scatters.

Year	DOY	UTC Time		T_{BWG}, K	RMS	T_{WVR}, K	RMS	T_{SURF}, K	$T_{BWG} - T_{WVR}$, K	$T_{BWG} - T_{SURF}$, K
		Start	End							
94	17	15:57	16:25	2.239	0.080	2.374	0.040	2.139	−0.135	0.100
94	17	22:30	22:47	2.239	0.059	2.388	0.032	2.138	−0.149	0.101
94	24	16:16	16:45	2.249	0.078	2.353	0.034	2.460	−0.104	−0.211
94	122	15:03	16:01	2.431	0.026	2.468	0.021	2.399	−0.037	0.032
94	122	21:42	22:41	2.338	0.047	2.461	0.089	2.196	−0.123	0.142
94	123	22:53	23:43	2.469	0.035	2.523	0.031	2.207	−0.054	0.262
94	124	05:09	06:00	2.467	0.016	2.540	0.026	2.400	−0.073	0.067
94	158	15:08	16:07	2.242	0.017	2.379	0.042	2.338	−0.137	−0.096
94	158	21:27	22:03	2.340	0.014	2.440	0.022	2.189	−0.100	0.151
94	178	22:43	23:11	2.700	0.016	2.654	0.048	2.322	0.046	0.378
94	199	15:18	15:33	2.905	0.065	2.779	0.025	2.411	0.126	0.494
94	220	14:59	15:24	2.796	0.012	2.718	0.016	2.283	0.078	0.513
94	229	23:18	23:37	3.154	0.096	3.030	0.028	2.869	0.124	0.285
94	255	22:42	23:05	2.354	0.057	2.383	0.083	2.259	−0.029	0.095
94	297	16:00	16:23	2.679	0.041	2.594	0.024	2.260	0.085	0.419
94	298	05:51	06:13	2.699	0.052	2.539	0.046	2.473	0.160	0.226
94	306	15:59	16:21	2.887	0.119	2.620	0.095	2.488	0.267	0.399
94	311	18:24	18:46	2.358	0.024	2.366	0.052	2.132	−0.008	0.226
94	325	18:50	19:14	2.386	0.031	2.351	0.016	2.105	0.035	0.281

in (1) and (2) above; then a conversion to reference to 8.4 GHz was applied,[10] and then the effective 8.4-GHz cosmic contribution was removed.

Based on an examination of the WVR scatters about the tip-curve intervals, the scatters at 32 GHz (see Table 4) for typical "dry" days range from 0.06 to 0.6 K and are in reasonable agreement with the BWG tip-curve postfit rms scatters. At 32 GHz, the few cases of significantly different scatters of the WVR data relative to the BWG data may be attributed to (1) the effects of averaging time and algorithm of the WVR, (2) cases of higher than usual gain instability for the BWG system, or (3) the difference in atmospheric noise between the regions of the sky observed with the BWG and WVR.

The average 13.2 K of T_{atm} at zenith for 32 GHz is in agreement with the 13.2 K of the WVR for this subset. The average of the difference temperatures between the BWG tip curve and the WVR is 0.06 ± 0.64 K, which is consistent with the 0.5-K absolute accuracy of the WVR.[11] As the WVR and BWG data were acquired in different parts of the sky, this agreement is indicative of the good weather conditions under which most of the KaAP experiments have been conducted. The average difference of the BWG atmospheric temperatures minus those of the surface model is 3.6 ± 2.5 K. If the BWG and WVR data are indicative of the true statistical weather conditions at Goldstone, then the surface model for Goldstone will require refinement. The 2.5-K average value of the BWG T_{atm} at zenith for 8.4 GHz over this subset is in agreement with the 2.5-K average value derived from the WVR data. The 8.4-GHz scatters about the fit of the BWG tip-curve data and the scatter of the WVR data over the tip-curve measurement

[10] S. Keihm, "Conversion of WVR 31.4 GHz Zenith TB Measurements to X-band," JPL Interoffice Memorandum 3833-94-440/SJK (internal document), Jet Propulsion Laboratory, Pasadena, California, December 15, 1994.

[11] S. Keihm, personal communication, Jet Propulsion Laboratory, Pasadena, California, May 1995.

period are usually in reasonable agreement (typically 0.03 K). The average of the temperature differences between BWG and WVR values for 8.4 GHz is -0.001 ± 0.12 K, while the corresponding average for the BWG relative to the surface model is 0.2 ± 0.2 K.

Previous work at 32 GHz by Otoshi et al. [9] at DSS 13 also found that their 32-GHz measurements significantly disagreed with values derived from the surface model. This was explained as being due to either (1) the theoretical weather model not being as good at 32 GHz as it was at 8.4 GHz or (2) the elevation-dependent noise contributions of the antenna being corrupted more from tripod leg scatter, spillover, and panel leakage. Based on these studies ([9] and this article), it appears that the surface weather model at 32 GHz for Goldstone requires refinement.

3. RMS Scatter About Fitted Model. The contributions to the rms noise in the BWG tip-curve post-fit residual temperatures are (1) thermal noise, (2) uncalibrated gain changes, (3) atmospheric noise, and (4) systematic mismodeling,

$$\sigma_T = T_{op}\sqrt{\frac{1}{B\tau} + \left(\frac{\Delta G}{G}\right)^2 + \frac{\sigma_{atm}^2}{T_{op}^2} + \frac{\sigma_{mod}^2}{T_{op}^2}}$$

where T_{op} is the operating temperature measurement (K), B is the radiometer bandwidth (Hz), τ is the radiometer integration time (s), $\Delta G/G$ is the normalized uncalibrated gain variation between minicals, σ_{atm} is the atmospheric fluctuation (K), and σ_{mod} is mismodeling noise (K).

Random fluctuations are expected to lie below 0.01 K given the noise bandwidths and integration time of the TPR. Uncalibrated gain fluctuations for most passes are expected to be on the order of 0.1 percent of the operating noise temperatures (0.04 K at 8.4 GHz and 0.07 K at 32 GHz) based on the gain changes observed between minicals. These levels appear to be consistent with many of the lower-value rms scatters in Tables 2 and 3. Higher values of rms scatters in Tables 2 and 3 are usually attributed to atmospheric fluctuations over the tip-curve interval, especially those observed during known turbulent weather conditions.

The major contribution to the rms noise at 32 GHz for the majority of the data sets is expected to be due to a small amount of systematic mismodeling of the temperature model. The quadratic model used for antenna temperature at 32 GHz, which is removed from the data [Eq. (5)], varies about 1.5 K from 10 deg to zenith (see Fig. 5), most of which is attributed to tripod scatter. The remaining ± 0.2-K signature seen in the postfit residuals (see Fig. 6) is more complex. The variation as the antenna moves off zenith is the unmodeled effect of the side lobes sweeping against the ground. The typical rms scatter of this effect over the typical tip-curve sequence is about 0.1 K at 32-GHz.

The elevation-dependent antenna temperature model used in this study at 32 GHz appears to be consistent within 0.5 K (the quoted accuracy of the WVR data used in the intercomparison with the tip-curve data). The good agreement of the BWG tip-curve data with the WVR data supports this. The smaller remaining signature of order 0.2 K visible in the postfit residuals at 32 GHz (see Fig. 6) was not considered significant to remove for the purpose of this first study. From the postfit residual plots of Fig. 6 and other tip-curve data sets, this systematic signature appears repeatable and can, therefore, be extracted from the data by using an appropriate model. As more data sets conducted in good weather are acquired, such a refinement in the model may be a possible output product of the data.

4. Cumulative Distributions of Atmospheric Noise Temperatures. Figure 15 is a plot of the cumulative distribution of the 32-GHz zenith atmospheric noise temperatures determined from the tip-curve data, and Fig. 16 is the corresponding plot for the 8.4-GHz values. Included on the plots are

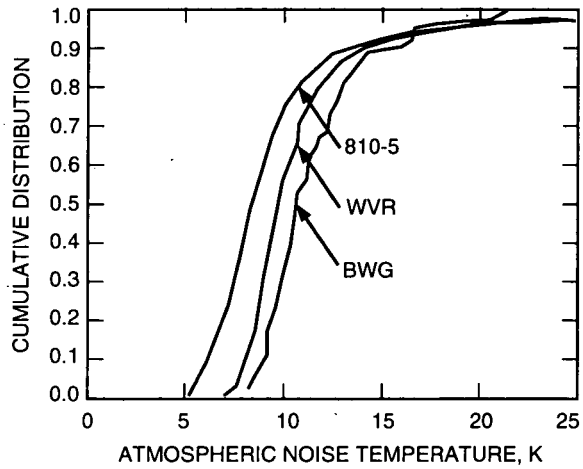

Fig. 15. Cumulative distribution of 32-GHz BWG tip-curve zenith atmospheric noise temperatures, WVR data, and 810-5 model.

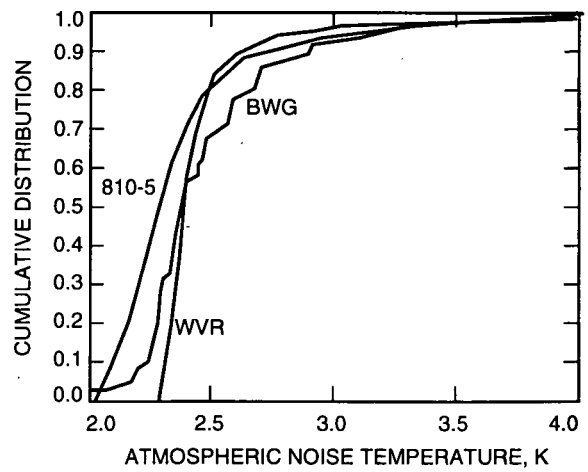

Fig. 16. Cumulative distribution of 8.4-GHz BWG tip-curve zenith atmospheric noise temperatures, WVR data, and 810-5 model.

the corresponding statistics derived from 31.4-GHz WVR data[12] (after removing the cosmic contribution and applying the necessary corrections to the appropriate frequency) and the cumulative statistics for Goldstone from a DSN design document referred to as 810-5.[13]

A few important points should be considered when interpreting these curves. First, all of the KaAP data points were acquired over a limited set of weather conditions that were mostly daytime observations conducted during prime shifts. The tip-curve and supporting surface meteorological data were indicative of observing conditions not spanning the full gamut of possible very dry or very wet conditions. The WVR statistics were determined from a virtually continuous set of R6 WVR data that covered a 10-month interval from October 6, 1993, to July 31, 1994 (not to be confused with the small subset of WVR data used in the previously discussed intercomparison). The 810-5 model was originally derived from data acquired at the overseas sites and then translated to reflect Goldstone conditions.[14] The surface model used in the intercomparison has statistics similar to the 810-5 model at 32 GHz. Figure 15 shows the 810-5 model's temperature for a given cumulative distribution (0.8 and under) significantly below those of the WVR and tip-curve-derived values at 32 GHz. The apparent biased 1-K lower value of the WVR over the BWG tip-curve values may reflect the fact that the WVR continuous data set was sampled over a greater number of drier periods than the fewer BWG tip curves, which were conducted primarily during daytime, when more water vapor may be present. Another possibility may be a bias error of order 1 K in one or both of the data acquisition systems and algorithms. As more DSS-13 BWG tipping-curve data sets are acquired over a longer time interval and over a wider range of weather conditions, a more meaningful characterization of the cumulative statistics can be realized.

V. Future Work

Efforts to further correlate the tipping-curve statistics with those of the WVR data should be performed as more BWG tipping-curve data are acquired. This will allow the availability of a large database of weather statistics derived from diverse equipment and data reduction methods. Such statistics will be useful to derive link strategies at 32 GHz for Goldstone.

---

[12] S. Keihm, "Goldstone 31.4 GHz WVR Statistics, October 93–July 94," JPL Interoffice Memorandum 3833-94-410/SJK (internal document), Jet Propulsion Laboratory, Pasadena, California, August 26, 1994.

[13] *Deep Space Network/Flight Project Interface Design Handbook, Volume I: Existing Capabilities*, 810-5, Rev. D (internal document), Module TCI-40, Jet Propulsion Laboratory, Pasadena, California, pp. 5–6, May 1, 1992.

[14] Ibid.

An improved elevation angle–dependent model for the antenna noise temperature at both 32 and 8.4 GHz should be estimated using the appropriate methodology and assumptions and then checked against the model derived from the data in this study. The estimate should characterize or set limits on the contribution of the tripod scatter. The tip-curve data (along with supporting WVR data) could be used to refine the antenna temperature versus elevation model at 32 GHz.

An updated, intensive, and careful analysis to estimate the loss factors of the antenna reflectors, mirrors, and tripod structures should be performed. The loss factors can change due to the amount of reflector or mirror misalignment present. Given that the original noise accounting budget was performed several years ago, a reassessment of these factors is in order.

Losses due to mismatch have not been considered in the analysis presented in this article. Future work should consider the effect of these losses in the temperature model and make use of any new values that become available from theoretical studies.

Acknowledgments

We thank R. Clauss, C. Stelzried, S. Stewart, L. Teitelbaum, P. Richter, S. Slobin, and G. Resch for several informative discussions and comments; the DSS-13 station personnel for acquiring data and promptly addressing data acquisition issues as they came up (L. Tanida, G. Bury, C. Goodson, R. Reese, J. Garnica, R. Littlefair, J. Crook, and C. Mitchell); C. Smyth and L. Lee for providing LMCOA capability; E. Paulsen, J. Bowen, S. Stewart, L. Alvarez, W. Veruttipong, and A. Bernardo for providing information on equipment and station specifications; S. Keihm for providing and interpreting the WVR data; and T. Rebold for assistance in software development.

References

[1] J. G. Smith, "Ka-Band (32-GHz) Downlink Capability for Deep Space Communications," *The Telecommunications and Data Acquisition Progress Report 42-88, October–December 1986*, Jet Propulsion Laboratory, Pasadena, California, pp. 96–103, February 15, 1987.

[2] J. W. Layland and J. G. Smith, "A Growth Path for Deep Space Communications," *The Telecommunications and Data Acquisition Progress Report 42-88, October–December 1986*, Jet Propulsion Laboratory, Pasadena, California, pp. 120–125, February 15, 1987.

[3] A. L. Riley, D. M. Hanson, A. Mileant, and R. W. Hartop, "A Ka-Band Beacon Link Experiment (KABLE) With Mars Observer," *The Telecommunications and Data Acquisition Progress Report 42-88, October–December 1986*, Jet Propulsion Laboratory, Pasadena, California, pp. 141–147, February 15, 1987.

[4] T. A. Rebold, A. Kwok, G. E. Wood, and S. Butman, "The Mars Observer Ka-Band Link Experiment," *The Telecommunications and Data Acquisition Progress Report 42-117, January–March 1994*, Jet Propulsion Laboratory, Pasadena, California, pp. 250–282, May 15, 1994.

[5] L. S. Alvarez, "Analysis and Applications of a General Boresight Algorithm for the DSS-13 Beam Waveguide Antenna," *The Telecommunications and Data Acquisition Progress Report 42-111, July–September 1992*, Jet Propulsion Laboratory, Pasadena, California, pp. 48-61, November 15, 1992.

[6] C. T. Stelzried and M. J. Klein, "Precision DSN Radiometer Systems: Impact on Microwave Calibrations," *Proc. of the IEEE*, vol. 82, pp. 776–787, May 1994.

[7] J. C. Chen, P. H. Stanton, and H. F. Reilly, "Performance of the X-/Ka-/KABLE-Band Dichroic Plate in the DSS-13 Beam Waveguide Antenna," *The Telecommunications and Data Acquisition Progress Report 42-115, July–September 1993*, Jet Propulsion Laboratory, Pasadena, California, pp. 54–64, November 15, 1993.

[8] S. J. Keihm, "Water Vapor Radiometer Measurements of the Tropospheric Delay Fluctuations at Goldstone Over a Full Year," *The Telecommunications and Data Acquisition Progress Report 42-122, April–June 1995*, Jet Propulsion Laboratory, Pasadena, California, pp. 1–11, August 15, 1995.

[9] T. Y. Otoshi, S. R. Stewart, and M. M. Franco, "A Portable Ka-band Front-End Test Package for BWG Antenna Performance Evaluation, Part II: Tests on the Antenna," *The Telecommunications and Data Acquisition Progress Report 42-106, April–June 1991*, Jet Propulsion Laboratory, Pasadena, California, pp. 266–282, August 15, 1991.

[10] S. D. Slobin, "Microwave Noise Temperature and Attenuation of Clouds: Statistics of these Effects at Various Sites in the United States, Alaska, and Hawaii," *Radio Science*, vol. 17, pp. 1443–1454, November–December 1982.

[11] M. L. Kutner, "Application of a Two-Layer Atmospheric Model to the Calibration of Millimeter Observations," *Astrophysical Letters*, vol. 19, pp. 81–87, 1978.

[12] T. Y. Otoshi, S. R. Stewart, and M. M. Franco, "A Portable X-band Front-End Test Package for BWG Antenna Performance Evaluation Part II: Tests on the Antenna," *The Telecommunications and Data Acquisition Progress Report 42-105, January–March 1991*, Jet Propulsion Laboratory, Pasadena, California, pp. 54–68, May 15, 1991.